CrossMark

Searching for Exotic Cores with Binary Neutron Star Inspirals

Hsin-Yu Chen , Paul M. Chesler, and Abraham Loeb
Black Hole Initiative, Harvard University, Cambridge, MA 02138, USA; hsinyuchen@fas.harvard.edu, pchesler@g.harvard.edu, aloeb@cfa.harvard.edu

Abstract

We study the feasibility of detecting exotic cores in merging neutron stars with ground-based gravitational-wave detectors. We focus on models with a sharp nuclear/exotic matter interface, and assume a uniform distribution of neutron stars in the mass range $[1, 2]\,M_\odot$. We find that the existence of exotic cores can be confirmed at the 70% confidence level with as few as several tens of detections. Likewise, with such a sample, we find that some models of exotic cores can be excluded with high confidence.

1. Introduction

The discovery of binary neutron star mergers (BNSs) by the Advanced Laser Interferometer Gravitational-Wave Observatory (LIGO)-Virgo (Abbott et al. 2017a) has ushered an era of multimessenger astronomy (Abbott et al. 2017b). BNSs also provide a unique laboratory to study the equation of state (EoS) of Quantum Chromodynamics (QCD) matter, which at densities beyond the nuclear saturation density is largely unknown. Already, the single event GW170817 indicates a relatively soft EoS (Abbott et al. 2018a, 2019). Advanced LIGO-Virgo is expected to observe tens to hundreds of BNSs in the next few years (Abbott et al. 2018b), substantially improving constraints on the EoS of dense QCD matter over time (see e.g., Annala et al. 2018; Most et al. 2018; Carson et al. 2019b; Forbes et al. 2019; Tews et al. 2019).

At densities beyond the nuclear saturation density, microscopic calculations of the EoS are increasingly uncertain and dense QCD matter is likely strongly coupled. Because of this, the nature of matter in the cores of NSs is largely inaccessible with current theoretical tools. An exciting possibility is the existence of exotic matter (EM) at high densities, including hyperonic and quark matter. This can result in hybrid neutron stars (HNSs), with an EM core surrounded by a mantle of nuclear matter (see e.g., Seidov 1971; Schaeffer et al. 1983; Lindblom 1998; Alford et al. 2001, 2013, 2019; Alford & Han 2016; Haensel et al. 2016; Yagi & Yunes 2017; Fortin et al. 2018; Annala et al. 2019; Montaña et al. 2019). EM can also be produced during post-merger dynamics (Most et al. 2019; Bauswein et al. 2019). A tantalizing question arises as to whether the effects of EM be observed with gravitational-wave (GW) detectors. If so, what are the observable signatures of EM? How many mergers must one observe before the presence of EM can be confidently established? These are the questions we seek to address.

We focus on EM scenarios most easily observable with current GW detectors. As no obvious sign of post-merger dynamics were recorded in GW170817, likely due to post-merger dynamics being outside of LIGO's frequency bandwidth, we choose to study the effects of HNSs during the inspiral phase of NS mergers. Additionally, we focus on HNSs with a sharp transition between nuclear and EM, meaning those without a mixed phase.

The presence of a EM core can have dramatic effects on mass–radius (MR) curves, with the nature of the modification depending on the discontinuity in the energy density (i.e., latent heat) and the speed of sound (Alford et al. 2013; Benic et al. 2015; Alford & Han 2016; Steiner et al. 2018). For illustrative purposes, Figure 1 shows the MR curve for the MPA1 nuclear EoS of Müther et al. (1987) together with hybrid MR curves generated via a constant sound speed EM EoS. If the latent heat is large (or the sound speed is small), HNSs are unstable to collapse and the stable branch of the MR curve terminates at some mass m_c, which is the mass where EM is first nucleated (Schaeffer et al. 1983; Lindblom 1998). For smaller latent heats (or larger sound speeds), the resulting HNSs can have both connected and disconnected MR curves. Crucial to our analysis is the fact that the slope of hybrid branch of the MR curve need not be the same as that of the nuclear branch.

We focus on mergers with component masses in the $[1, 2]\,M_\odot$ range. There are two reasons for doing this. First, the heaviest observed neutron stars (NSs) have masses $2.01 \pm 0.04\,M_\odot$ (Antoniadis et al. 2013) and $2.17 \pm 0.1\,M_\odot$ (Cromartie et al. 2020). Because $2\,M_\odot$ NSs are evidently stable, astrophysical processes such as supernova and NS mergers presumably cannot produce black holes lighter than $2\,M_\odot$. Likewise, $\mathcal{O}(M_\odot)$ primordial black holes are not expected to be abundant (see, for example, Carr & Kuhnel 2019). It is therefore reasonable to surmise that all mergers with components in the $[1, 2]\,M_\odot$ range are BNSs. If the BNS detections are contaminated by neutron star–black hole mergers, significant biases in measured radii can be introduced (Chen & Chatziioannou 2019). Second, in the $[1, 2]\,M_\odot$ range the vast majority of viable nuclear EoS yield roughly constant MR curves (see, for example, Figure 10 of Ozel & Freire 2016). This should be contrasted with the kink at critical mass m_c shown in Figure 1. Restricting our attention to the $[1, 2]\,M_\odot$ range therefore allows us to use abrupt changes in MR curves—kinks—as an identifier for exotic cores, with the location of the kink corresponding to the critical mass m_c. As we shall see below, kinks in MR curves readily manifests themselves in GW observables, and can be seen with a large enough collection of events.

2. Simulations

We construct an ensemble of simulated BNSs. Input data consists of the NS masses m_1 and m_2 and the NS MR curve. As the mass distribution of NSs outside the Milky Way is unknown, we choose m_1 and m_2 uniformly distributed in $[1, 2]$ $M_\odot$, with $m_1 \geqslant m_2$. Additional GW observables we employ are
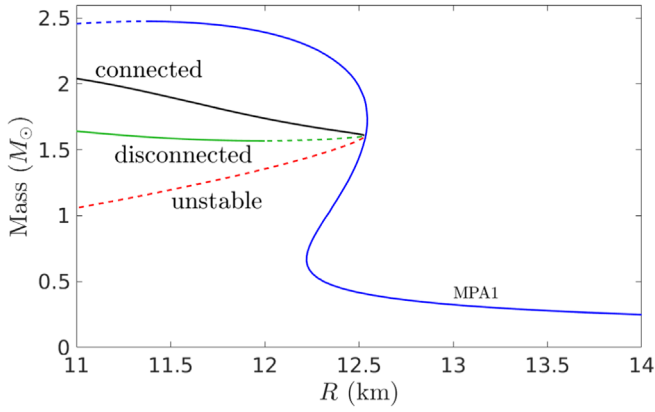
Figure 1. An example of MR curves with and without EM. The critical mass for the hybrid branch is $m_c = 1.6\,M_\odot$, beyond which EM cores exists. Regions with positive slope are unstable and shown as dashed lines.

the chirp mass $\mathcal{M} \equiv (m_1 m_2)^{3/5}/(m_1 + m_2)^{1/5}$, and the mass weighted tidal deformability

$$\widetilde{\Lambda} \equiv \frac{16}{13} \frac{(m_1 + 12m_2)m_1^4 \Lambda_1 + (m_2 + 12m_1)m_2^4 \Lambda_2}{(m_1 + m_2)^5}, \quad (1)$$

where Λ_1 and Λ_2 are the tidal deformabilities of the individual NSs. $\widetilde{\Lambda}$ is determined from the MR curve and the masses m_1 and m_2. This follows from the universal relationship between each NS's compactness $C \equiv m/R$, and tidal deformability Λ, which reads (Maselli et al. 2013; Yagi & Yunes 2017)

$$C = a_0 + a_1 \log\Lambda + a_2 \log^2 \Lambda, \quad (2)$$

where $a_0 = 0.3617$, $a_1 = -0.03548$ and $a_2 = 6.194 \times 10^{-4}$. Equation (2) holds at the 7% level or better for both purely nuclear NSs and HNSs (Carson et al. 2019a). Equation (2) can be inverted to find $\Lambda(C)$, which upon substituting into Equation (1) yields $\widetilde{\Lambda}$ in terms of m_1 and m_2 and the NS radii R_1 and R_2. Because Equation (2) is insensitive to the underlying EoS, we can directly apply it to the MR curves employed in the following two paragraphs to obtain $\widetilde{\Lambda}$ for a given BNS with mass (m_1, m_2).

Our analysis below is unable to resolve detailed structure in MR curves. For simplicity, we therefore employ piecewise linear MR curves. For nuclear MR curves we use $R_{\rm nuclear}(m) = \mathcal{R}(m|p_0, p_1, p_2, p_3)$ where

$$\mathcal{R}(m|p_0, p_1, p_2, p_3) \equiv \begin{cases} p_2(m - p_1) + p_0, & m < p_1, \\ p_3(m - p_1) + p_0, & m \geqslant p_1. \end{cases} \quad (3)$$

We employ eight sets of parameters p_i (models A–H) listed in Table 1, with the associated MR curves plotted in Figure 2. Note that our analysis below is insensitive to overall radial shifts (i.e., the parameter p_0). For comparison, also shown in the figure are several MR curves obtained from Müther et al. (1987), Douchin & Haensel (2001), Akmal et al. (1998), Alford et al. (2005). Note that models E–H approximate these MR curves.

We focus on HNS with connected MR curves with

$$R_{\rm hybrid}(m) \equiv \begin{cases} R_{\rm nuclear}(m), & m < m_c, \\ \alpha(m - m_c) + R_{\rm nuclear}(m_c), & m \geqslant m_c, \end{cases} \quad (4)$$
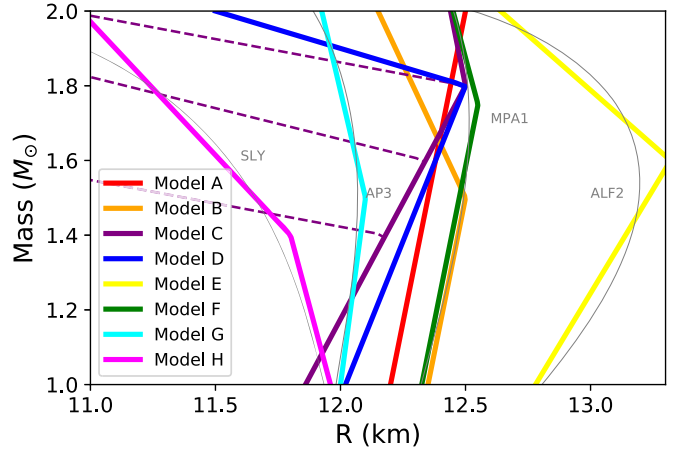
Figure 2. Eight linear piecewise models for $R_{\rm nuclear}(m)$. For comparison, the MR curves generated with several candidate nuclear EoS are also shown. The purple dashed lines correspond to several hybrid branches of the MR curves.

Table 1
Parameters Chosen for Our Nuclear MR Curves

Model	p_0(km)	$p_1\ (M_\odot)$	p_2 (km $M_\odot^{-1}$)	p_3(km $M_\odot^{-1}$)
A	12.5	2.0	0.3	0.0
B	12.5	1.5	0.3	−0.7
C	12.5	1.8	0.8	−0.3
D	12.5	1.8	0.6	−5.0
E	13.32	1.6	0.9	−1.7
F	12.55	1.75	0.3	−0.4
G	12.1	1.5	0.2	−0.35
H	11.8	1.4	−0.4	−1.4

with critical mass m_c and hybrid branch slope α

$$m_c = \{1.2, 1.4, 1.6, 1.8\}M_\odot, \quad (5a)$$

$$-\alpha = \{0.5, 1, 2, 4, 6, 8, 10\}\ {\rm km}\,M_\odot^{-1}. \quad (5b)$$

We use the same parameters p_i listed in Table 1 and refer to hybrid MR curves as "hybrid models A–H with hybrid branch slope α and critical mass m_c."[1] Also shown in Figure 2 are several hybrid branches for model C.

The signal-to-noise ratio (S/N) of the simulated detections follows a power-law distribution valid for nearby events with redshift less than ∼0.1 (see Schutz 2011; Chen & Holz 2014 for details). For each merger we use the S/N to add Gaussian noise to the *inferred* radius, Equation (6) below, and masses m_1 such that a GW170817-like event has 1σ radius and mass uncertainties of 0.75 km and $0.1\,M_\odot$, respectively (Abbott et al. 2018a, 2019). The chirp mass is assumed to be measured with negligible uncertainty.
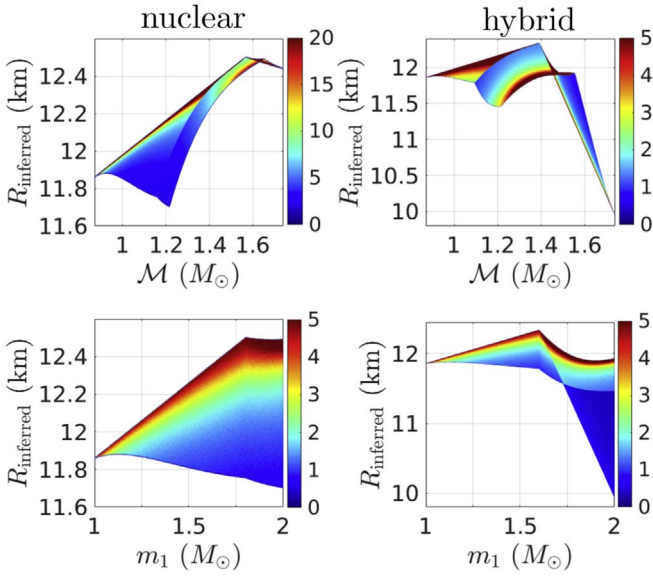
3. Data Analysis and Results

A useful observable to analyze data is the *inferred* radius,

$$R_{\rm inferred}(\mathcal{M}, \widetilde{\Lambda}) \equiv 2^{1/5}\mathcal{M}/C(\widetilde{\Lambda}), \quad (6)$$

where $C(\Lambda)$ is given by Equation (2). Note that in the special case $m_1 = m_2$, Equations (1) and (2) imply $R_1 = R_2 = R_{\rm inferred}$.

---

[1] Some of the parameter combinations could lead to hybrid models with radii less than the Schwarzschild radii. We removed these models in our study.

Figure 3. Density of events in the $\mathcal{M}$–R_{inferred} (top row) and m_1–R_{inferred} (bottom row) planes for nuclear model C (left panels) and a hybrid model (right panels) with hybrid branch slope $\alpha = -6$ and critical mass $m_c = 1.6\,M_\odot$. Outside the shaded regions the densities vanish. Note the presence of kinks in the hybrid allowed regions, which occur at $\mathcal{M} = m_c/2^{1/5}$ and $m_1 = m_c$.

For our analysis, the utility of R_{inferred} lies in the fact that it is sensitive to kinks in MR curves. To illustrate this, in Figure 3 we show the density of events in the $\mathcal{M}$–R_{inferred} (top) and m_1–R_{inferred} (bottom) planes for nuclear model C (left) and hybrid model C with critical mass $m_c = 1.6\,M_\odot$ and hybrid branch slope $\alpha = -6$ km $M_\odot^{-1}$. The density of events vanishes outside the shaded regions.[2] As is evident from the figure, HNSs produce pronounced kinks in allowed regions, with negative slopes at larger $\mathcal{M}$ and m_1. In contrast, the allowed regions generated by nuclear model C show no prominent kinks or pronounced downward trends as $\mathcal{M}$ or m_1 increase.

A simple scheme to search for kinks in the $\mathcal{M}$–R_{inferred} and m_1–R_{inferred} planes is to fit the data to linear piecewise models $\mathcal{R}(\mathcal{M}|\mathcal{P}_0, \mathcal{P}_1, \mathcal{P}_2, \mathcal{P}_3)$ and $\mathcal{R}(m_1|P_0, P_1, P_2, P_3)$, respectively, with fit parameters $\mathcal{P}_i$ and P_i, and $\mathcal{R}$ given by Equation (3).[3] As an example, in Figure 4 we show one realization of 40 detections in the measured $\mathcal{M}$–R_{inferred} plane (left panel) and the measured m_1–R_{inferred} plane (right panel) for the hybrid model shown in Figure 3. Also shown are the associated piecewise fits. We find that after repeating our simulations 500 times with 40 detections in each simulation, the majority of the simulations with HNSs return negative slope $\mathcal{P}_3$. This is in qualitative agreement with the shape of the allowed region in the $\mathcal{M}$–R_{inferred} plane shown in Figure 3 for hybrid data.

In Figure 5, we show the fraction of 500 simulated ensembles that return $\mathcal{P}_3 < 0$ with hybrid injection data with slope α and critical mass m_c. In each ensemble there are 40 simulated events. This quantity measures the confidence a hybrid model with parameters m_c and α can be excluded if $\mathcal{P}_3 > 0$ with 40 BNS
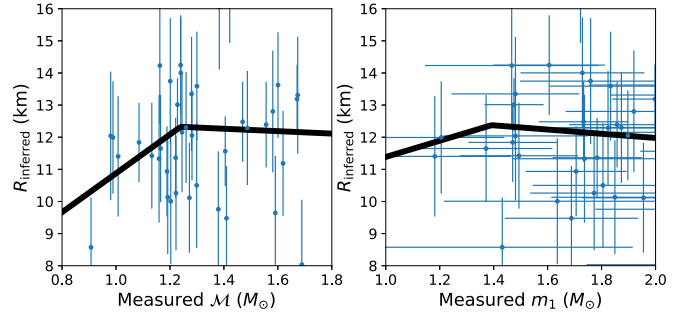
Figure 4. Left panel: an example of 40 simulated events in the $\mathcal{M}$–R_{inferred} plane for the same hybrid model shown in Figure 3. Right panel: the same thing but in the m_1–R_{inferred} plane. The solid lines in both plots are piecewise linear fits.
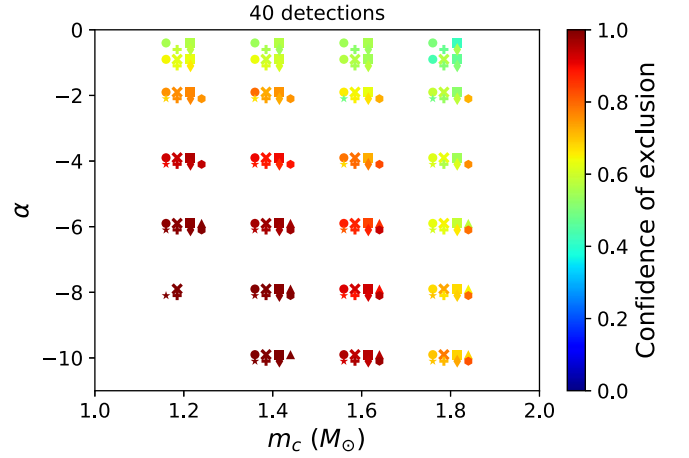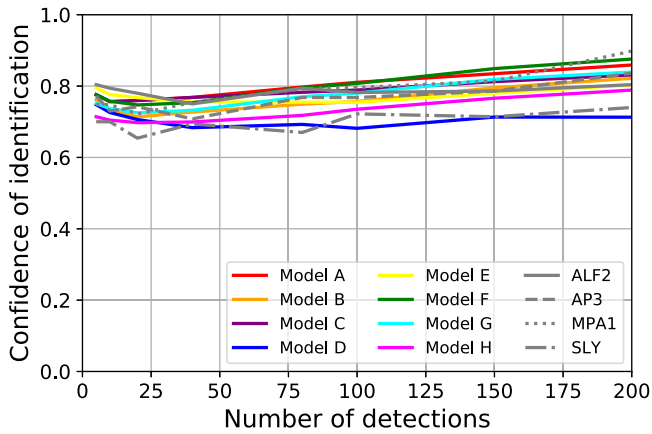

Figure 5. Confidence of exclusion for hybrid models as function of critical mass m_c and slope α. The eight symbols represent our eight choices of parameters p_0 and p_2, which are the same as those listed in Table 1, with circle: model A, cross: model B, square: model C, triangle: model D, star: model E, plus: model F, diamond: model G, and hexagon: model H.

detections. As is evident from the figure, smaller critical masses m_c and more negative slopes α can be excluded with greater confidence than larger m_c and/or more positive α. This is due to the fact that more negative α produce larger kinks in the allowed regions in the $\mathcal{M}$–R_{inferred} plane, making $\mathcal{P}_3$ more negative. Likewise, larger m_c leaves fewer events in the [1, 2] $M_\odot$ range with masses $>m_c$, making the associated downward trend more difficult to resolve. Nevertheless, it is noteworthy that already with 40 detections, hybrid models with $m_c \leqslant 1.6\,M_\odot$ and $\alpha \leqslant -6$ km $M_\odot^{-1}$ can be excluded at $>80\%$ confidence level if $\mathcal{P}_3 > 0$.

On the other hand, with injection data from nuclear models A–H, we find that the majority of our simulations return measured $\mathcal{M}$ slope $\mathcal{P}_3 > 0$ or measured m_1 slope discontinuity P_2–$P_3 < 1$ km $M_\odot^{-1}$. This selection criterion matches Figure 3, where the nuclear model produced upward trends in the $\mathcal{M}$–R_{inferred} plane as $\mathcal{M}$ increases and no kinks in the m_1–R_{inferred} plane. In Figure 6 we plot unity minus the fraction of simulated nuclear ensembles that return $\mathcal{P}_3 < 0$ and P_2–$P_3 > 1$ km $M_\odot^{-1}$ as a function of the number of events in each ensemble. This quantity can be interpreted as the confidence level of identifying an HNS. Figure 6 shows the confidence of identifying HNS as a function of the number of detections. Also shown in the figure is the confidence of

Figure 6. Confidence of identification of HNSs as a function of the number of detections with our eight different nuclear models as well as the ALF2, AP3, MPA1, and SLY EoS.
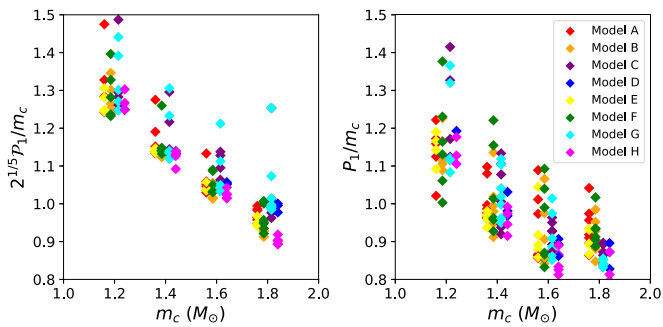
Figure 7. Estimate of critical mass normalized to the injected value, $2^{1/5}\mathcal{P}_1/m_c$ (left) and P_1/m_c (right), as a function of injected critical mass m_c, from 200 detections identified as having HNSs with our selection criterion.

identification for ALF2, AP3, MPA1, and SLY EoS, which agrees with that obtained from their piecewise linear approximates. Note the confidence of identification does not increase much as the number of events increases (and in fact even decreases slightly). This is due to our strict selection criteria, chosen to prevent misidentification of HNS, as well as the fact that our piecewise linear fits only qualitatively describes the distributions shown in Figure 3. Nevertheless, for the most pessimistic nuclear model, model D, we can construct over 70% confidence of identification with 40 observations if the observations return $\mathcal{P}_3 < 0$ and $P_2–P_3 > 1$ km $M_\odot^{-1}$. As we do not know the actual nuclear MR curve, the results from model D can be conservatively taken as the confidence of identification when our method is applied to real data.

We conclude our analysis by discussing the reconstruction of the critical mass m_c from our simulated data. From Figure 3 we see that kinks in the allowed regions in the $\mathcal{M}–R_{\text{inferred}}$ and $m_1–R_{\text{inferred}}$ plane occur at $\mathcal{M} = m_c/2^{1/5}$ and $m_1 = m_c$, respectively. Therefore, for simulations that are identified as having HNSs, $2^{1/5}\mathcal{P}_1$ and P_1 provide a rough estimate of m_c. In Figure 7, we show $2^{1/5}\mathcal{P}_1/m_c$ and P_1/m_c as a function of the injected critical mass m_c, averaged over 500 simulations, each with 200 mergers. The standard deviation of $\mathcal{P}_1$ is 0.05–0.7 $M_\odot$, while the standard deviation of P_1 is 0.2–0.6 $M_\odot$. In addition to the large statistical uncertainty, the figure also shows an estimate of the systematic errors. While the statistical uncertainty decreases over the number of detections, the systematic errors

remain. Again, this is because our piecewise linear fits only qualitatively describes the distributions shown in Figure 3.

4. Discussion

While we have focused only on HNS with connected MR curves, we have also studied those disconnected MR curves. In this case the allowed regions in the $\mathcal{M}–R_{\text{inferred}}$ and $m_1–R_{\text{inferred}}$ planes have gaps, which reflect the presence of gaps in the associated MR curves. Our present analysis cannot resolve these gaps, but it can resolve the change in slope associated with the formation of a core with similar fidelity as reported above for connected models. In the future, it would also be interesting to study the models with a mixed phase of nuclear and quark-matter. This scenario arises when the nuclear/quark matter surface tension is small (Alford et al. 2001). The presence of a mixed phase should soften kinks in MR curves, and correspondingly those in the $m_1–R_{\text{inferred}}$ and $\mathcal{M}–R_{\text{inferred}}$ planes. It remains to be seen how soft of a kink our analysis can detect.

We note that the selection criterion used to identify HNSs is not unique. While using a stronger selection criterion might, for a given number of events, identify HNSs with greater confidence, it might also misidentify more HNSs as nuclear than a weaker criterion.

There is plenty of room to improve our data analysis. First, we assumed a uniform NS mass distribution between $[1, 2]\,M_\odot$. Employing a different mass distribution will affect the fidelity in which HNS can be probed. For example, if $m_c = 1.6\,M_\odot$ and the NS mass distribution is narrowly distributed about $1.4\,M_\odot$, identifying EM cores will be very difficult due to few high-mass events. As more and more gravitational wave events are detected, the mass distribution should be better understood, and our analysis can be adjusted accordingly.

Additionally, our analysis of data in the $\mathcal{M}–R_{\text{inferred}}$ and $m_1–R_{\text{inferred}}$ planes can likely be improved. For example, instead of fitted data to piecewise linear *curves* $\mathcal{R}(\mathcal{M}|\mathcal{P}_0, \mathcal{P}_1, \mathcal{P}_2, \mathcal{P}_3)$ and $\mathcal{R}(m_1|P_0, P_1, P_2, P_3)$, it may be fruitful to fit instead to the *density* of expected events, which is determined by the mass distribution and the MR curve. This requires knowledge of the NS mass distribution. Fitting to the density of events can likely ameliorate the aforementioned systematic errors on the measurement of the critical mass.

ORCID iDs

Hsin-Yu Chen ⓘ https://orcid.org/0000-0001-5403-3762
Abraham Loeb ⓘ https://orcid.org/0000-0003-4330-287X

References

Abbott, B. P., Abbott, R., Abbott, T. D., et al. 2017a, PhRvL, 119, 161101
Abbott, B. P., Abbott, R., Abbott, T. D., et al. 2017b, ApJL, 848, L12
Abbott, B. P., Abbott, R., Abbott, T. D., et al. 2018a, PhRvL, 121, 161101
Abbott, B. P., Abbott, R., Abbott, T. D., et al. 2018b, LRR, 21, 3
Abbott, B. P., Abbott, R., Abbott, T. D., et al. 2019, PhRvX, 9, 011001
Akmal, A., Pandharipande, V. R., & Ravenhall, D. G. 1998, PhRvC, 58, 1804
Alford, M., Braby, M., Paris, M. W., & Reddy, S. 2005, ApJ, 629, 969

Alford, M. G., & Han, S. 2016, EPJA, 52, 62
Alford, M. G., Han, S., & Prakash, M. 2013, PhRvD, 88, 083013
Alford, M. G., Han, S., & Schwenzer, K. 2019, JPhG, 11, 114001
Alford, M. G., Rajagopal, K., Reddy, S., & Wilczek, F. 2001, PhRvD, 64, 074017
Annala, E., Gorda, T., Kurkela, A., Nättilä, J., & Vuorinen, A. 2019, arXiv:1903.09121
Annala, E., Gorda, T., Kurkela, A., & Vuorinen, A. 2018, PhRvL, 120, 172703
Antoniadis, J., Freire, P. C. C., Wex, N., et al. 2013, Sci, 340, 448
Bauswein, A., Bastian, N.-U. F., Blaschke, D. B., et al. 2019, PhRvL, 122, 061102
Benic, S., Blaschke, D., Alvarez-Castillo, D. E., Fischer, T., & Typel, S. 2015, A&A, 577, A40
Carr, B., & Kuhnel, F. 2019, PhRvD, 99, 103535
Carson, Z., Chatziioannou, K., Haster, C.-J., Yagi, K., & Yunes, N. 2019a, PhRvD, 99, 083016
Carson, Z., Steiner, A. W., & Yagi, K. 2019b, PhRvD, 100, 023012
Chen, H.-Y., & Chatziioannou, K. 2019, arXiv:1903.11197
Chen, H.-Y., & Holz, D. E. 2014, arXiv:1409.0522
Cromartie, H. T., Fonseca, E., Ransom, S. M., et al. 2020, NatAs, 4, 72
Douchin, F., & Haensel, P. 2001, A&A, 380, 151
Forbes, M. M., Bose, S., Reddy, S., et al. 2019, PhRvD, 100, 083010
Fortin, M., Oertel, M., & Providência, C. 2018, PASA, 35, 44
Haensel, P., Bejger, M., Fortin, M., & Zdunik, L. 2016, EPJA, 52, 59
Lindblom, L. 1998, PhRvD, 58, 024008
Maselli, A., Cardoso, V., Ferrari, V., Gualtieri, L., & Pani, P. 2013, PhRvD, 88, 023007
Montaña, G., Tolós, L., Hanauske, M., & Rezzolla, L. 2019, PhRvD, 99, 103009
Most, E. R., Papenfort, L. J., Dexheimer, V., et al. 2019, PhRvL, 122, 061101
Most, E. R., Weih, L. R., Rezzolla, L., & Schaffner-Bielich, J. 2018, PhRvL, 120, 261103
Müther, H., Prakash, M., & Ainsworth, T. L. 1987, PhLB, 199, 469
Ozel, F., & Freire, P. 2016, ARA&A, 54, 401
Schaeffer, R., Zdunik, L., & Haensel, P. 1983, A&A, 126, 121
Schutz, B. F. 2011, CQGra, 28, 125023
Seidov, Z. F. 1971, SvA, 15, 347
Steiner, A. W., Heinke, C. O., Bogdanov, S., et al. 2018, MNRAS, 476, 421
Tews, I., Margueron, J., & Reddy, S. 2019, EPJA, 55, 97
Yagi, K., & Yunes, N. 2017, PhR, 681, 1